PNAS

Supporting Information for

Arctic amplification induced decline in West and South Asia dust warrants stronger anti-desertification towards carbon neutrality

Fan Wang, Yangyang Xu, Piyushkumar N. Patel, Ritesh Gautam, Meng Gao, Cheng Liu, Yihui Ding, Haishan Chen, Yuanjian Yang, Yuyu Zhou, Gregory R. Carmichael, Michael B. McElroy

Corresponding author: Meng Gao and Cheng Liu

Email: mmgao2@hkbu.edu.hk (M.G.); chliu81@ustc.edu.cn (C.L.)

This PDF file includes:

Figures S1 to S18
Tables S1 to S5
SI Reference

Figures and Tables

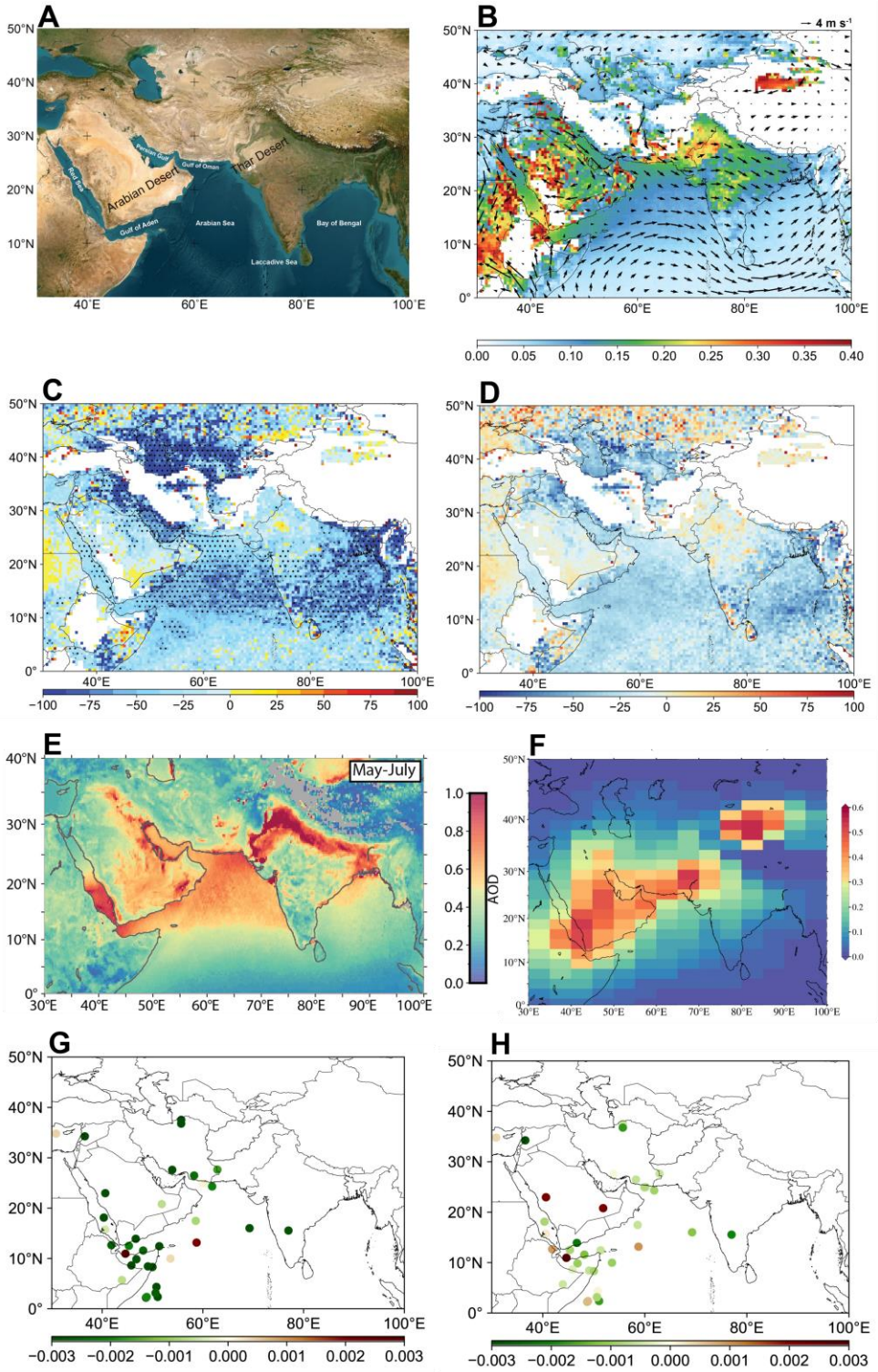

Figure S1. Topographic map, spatial distribution of DOD, atmospheric circulation and DOD changes. (A) Topographic map of West and South Asia. (B) Spatial distribution of DOD and wind vectors at 850 hPa. (C) Spatial distribution of DOD percentage changes from 2008 to 2019. Black dots denote areas with significant trend ($p < 0.05$). (D) Spatial distribution of percentage changes

of DOD from the Pre-period (2008-2013) to the Post-period (2014-2019). (E) Spatial distribution of MODIS AOD. (F) Spatial distribution of CALIOP DOD. (G) Spatial distribution of AERONET total AOD trend (1 per year) from 2008 to 2019. (H) Spatial distribution of AERONET coarse mode AOD trend (1 per year) from 2008 to 2019.

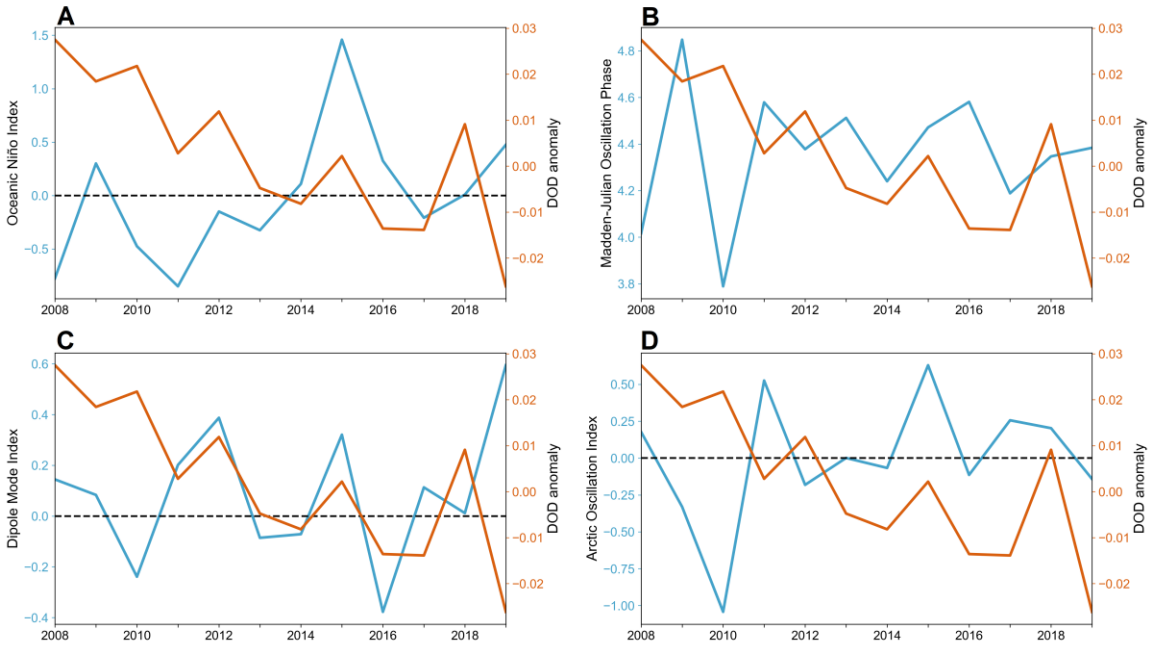

Figure S2. Variations of DOD anomalies and meteorological oscillations. Time series of DOD anomalies and Oceanic Niño Index (A), Madden-Julian Oscillation Phase (B), Dipole Mode Index (C) and Arctic Oscillation Index (D) over the 2008-2019 period. Data were taken from the Climate Prediction Center (https://www.cpc.ncep.noaa.gov/).

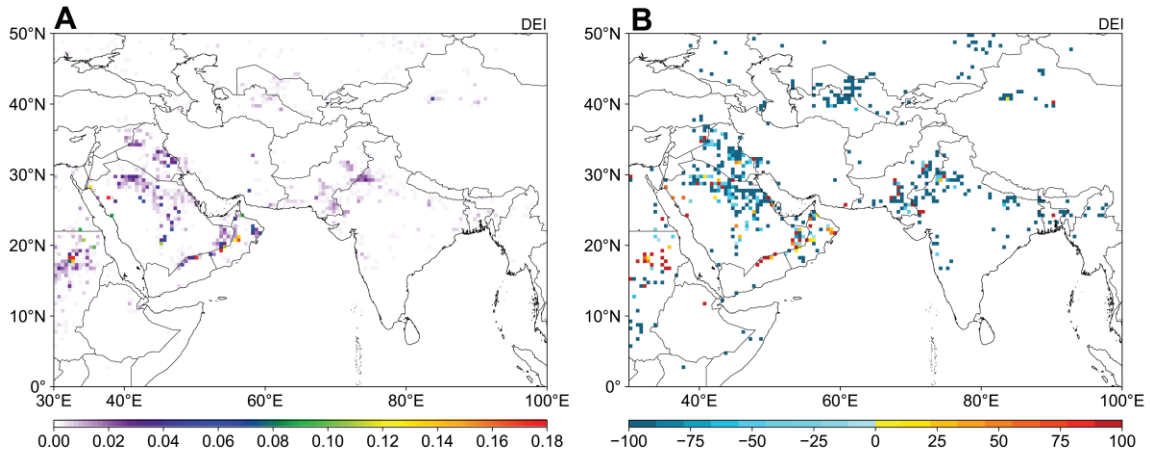

Figure S3. Spatial distribution of dust emission index (DEI) and its changes. (A) Spatial distribution of average DEI over the 2008-2019 period. (B) Spatial distribution of percentage changes of DEI from the Pre-period to the Post-period.

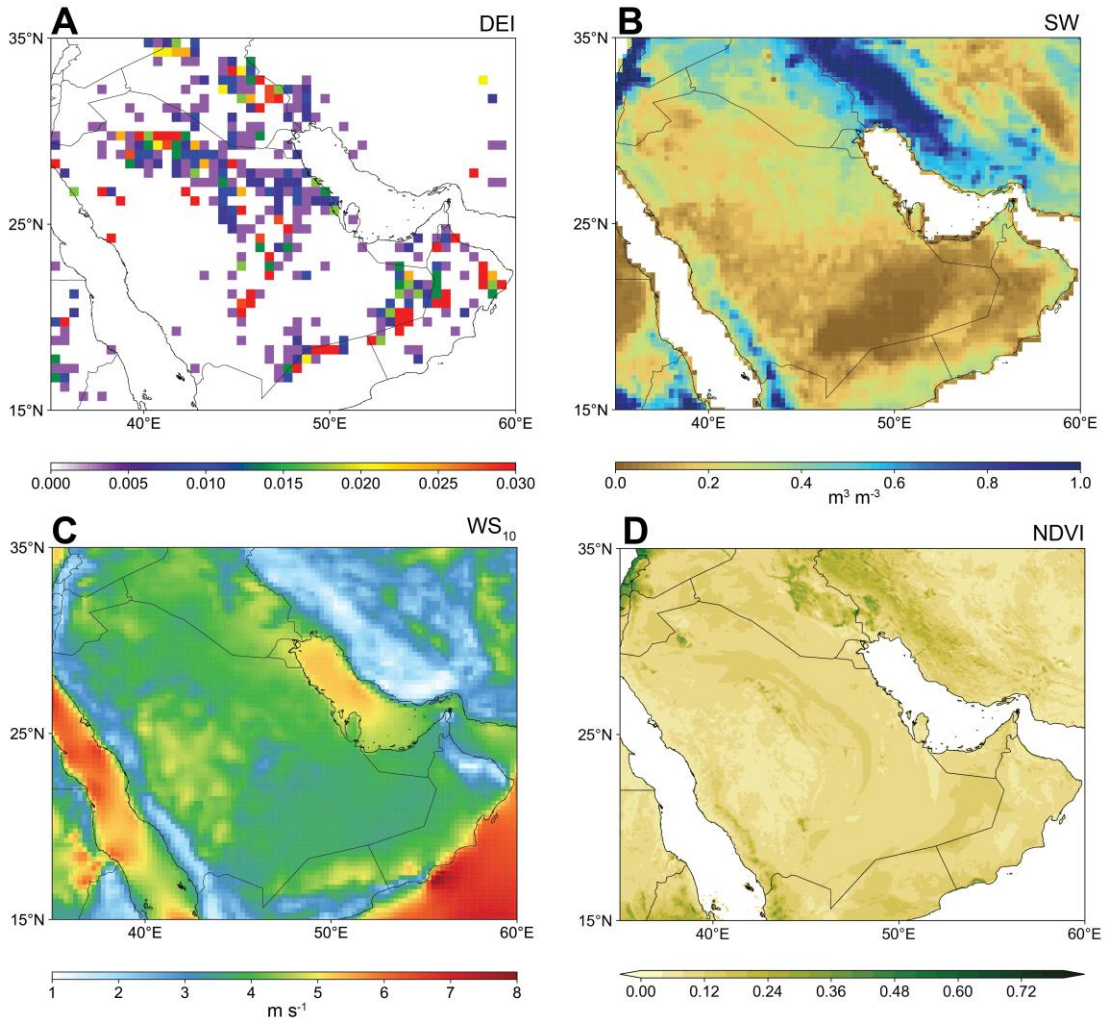

Figure S4. Spatial distribution of average patterns in West Asia. Spatial distribution of (A) average DEI, (B) soil water (SW), (C) 10m winds speed (WS_{10}) and (D) normalized difference vegetation index (NDVI) over the 2008-2019 period.

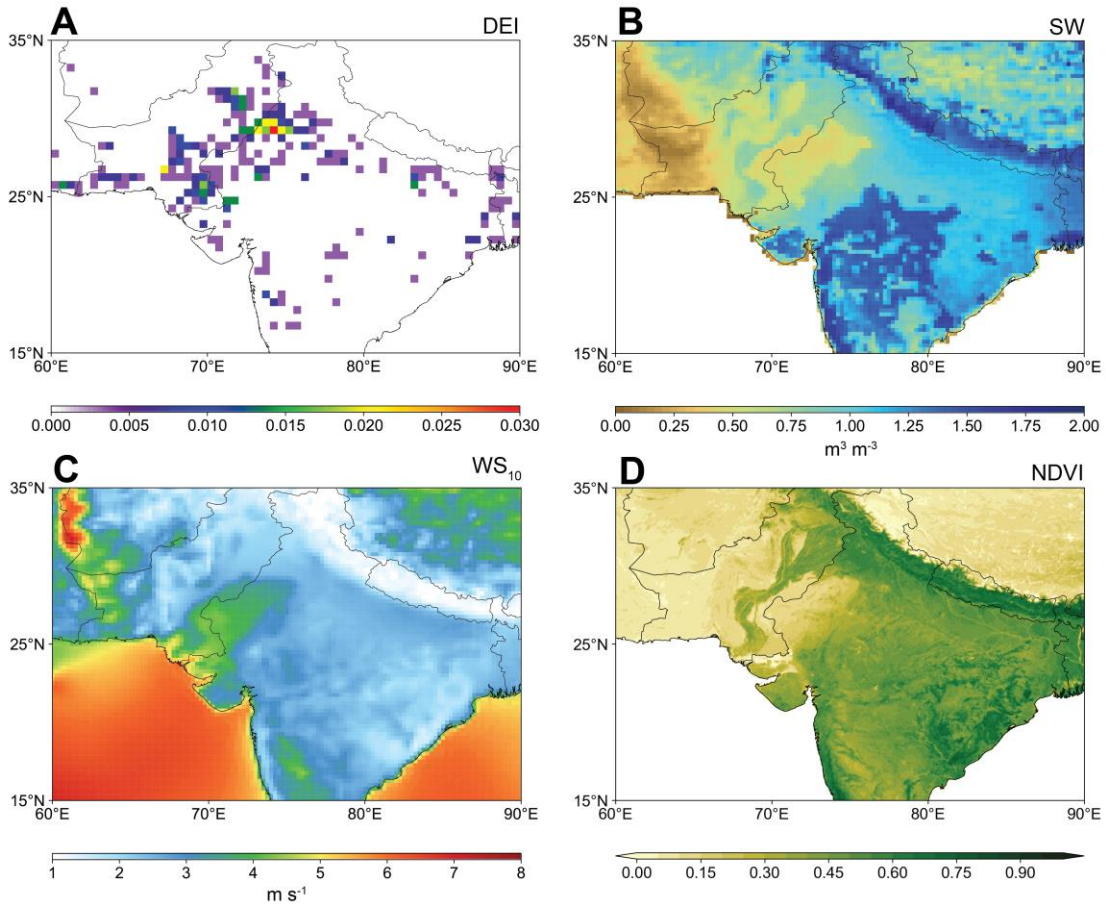

Figure S5. Spatial distribution of average patterns in South Asia. Spatial distribution of (A) average DEI, (B) soil water (SW), (C) 10m winds speed (WS_{10}) and (D) normalized difference vegetation index (NDVI) over the 2008-2019 period.

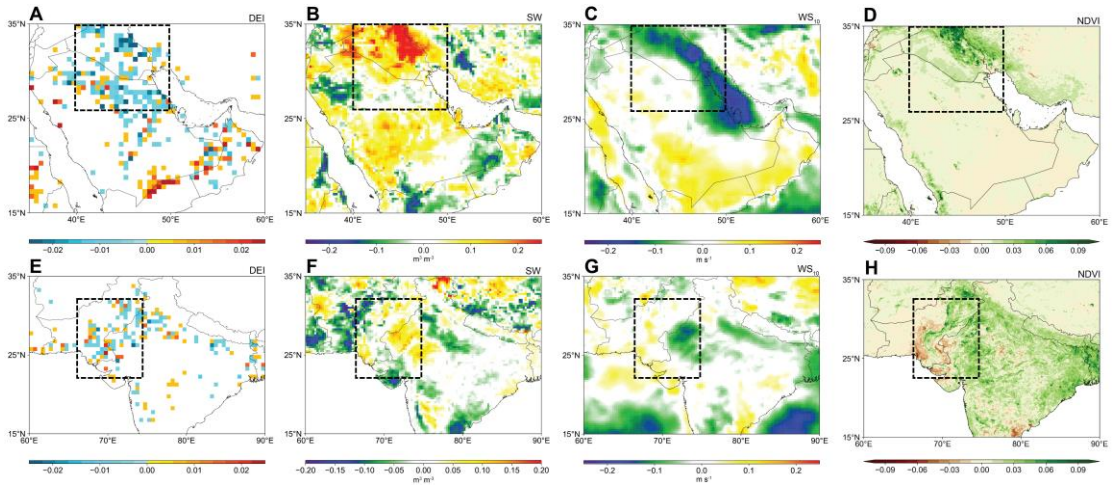

Figure S6. Dust emission index (DEI), soil water (SW), 10m winds speed (WS_{10}) and normalized difference vegetation index (NDVI) changes. Spatial distribution of (A) DEI, (B) SW, (C) WS_{10} and (D) NDVI changes from the Pre-period to the Post-period in West Asia. Spatial distribution of (E) DEI, (F) SW, (G) WS10 and (H) NDVI evolutions in South Asia. Black dashed squares indicate major dust source regions.

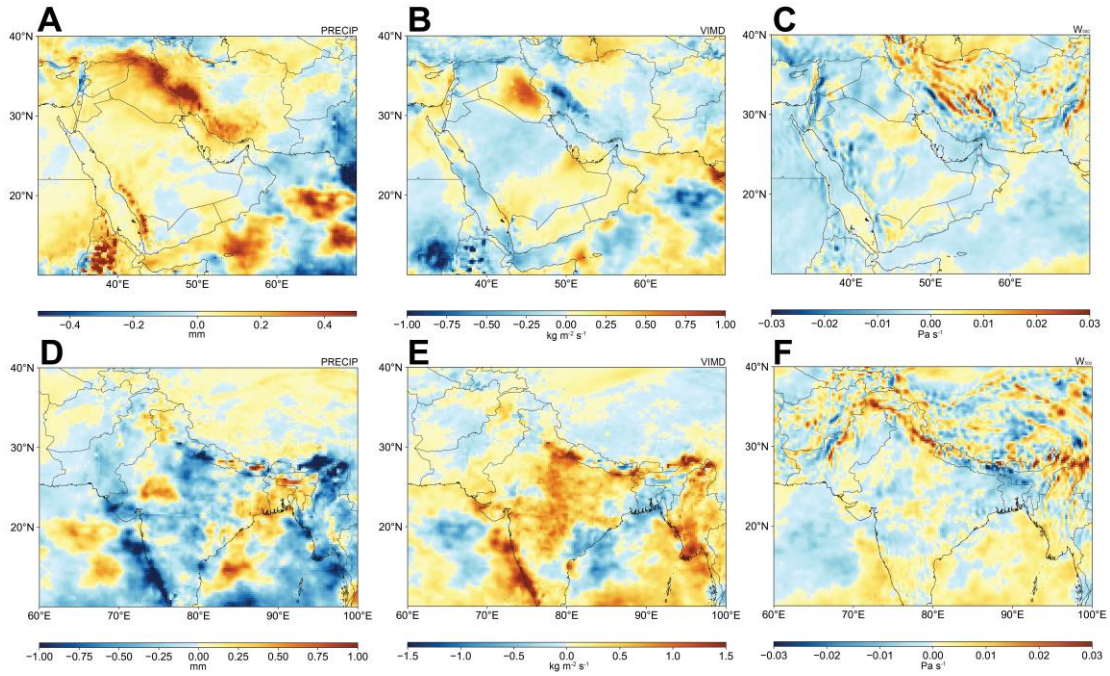

Figure S7. Spatial distribution of precipitation, vertically integrated moisture divergence and vertical velocity changes. Spatial distribution of (A) total precipitation (PRECIP), (B) vertically integrated moisture divergence (VIMD) and (C) vertical velocity at 500 hPa (W_{500}) changes from Pre-period to Post-period in West Asia. Spatial distribution of (D) PRECIP, (E) VIMD and (F) W_{500} changes from the Pre-period to the Post-period in South Asia.

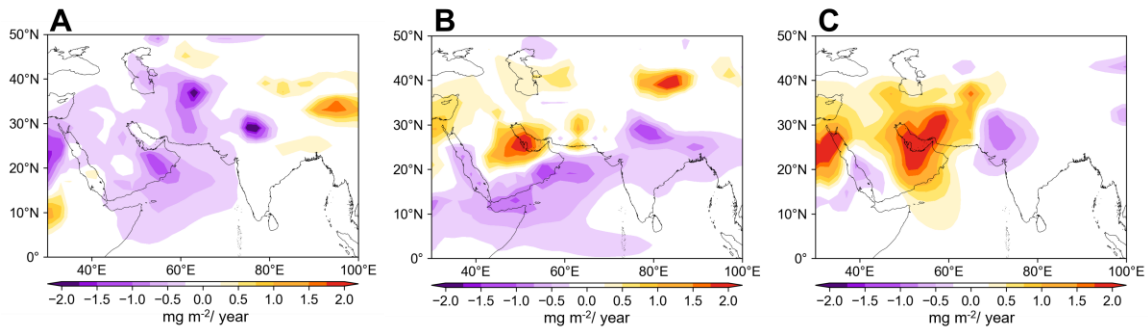

Figure S8. Spatial distribution of dust trends. Spatial distribution of dust trends from 2008 to 2019 in West and South Asia from historical from GHG-only (A) and aerosols-only (B) forcing experiments. (C) Spatial distribution of dust trends from 2008 to 2014 in West and South Asia from land use-only forcing experiments.

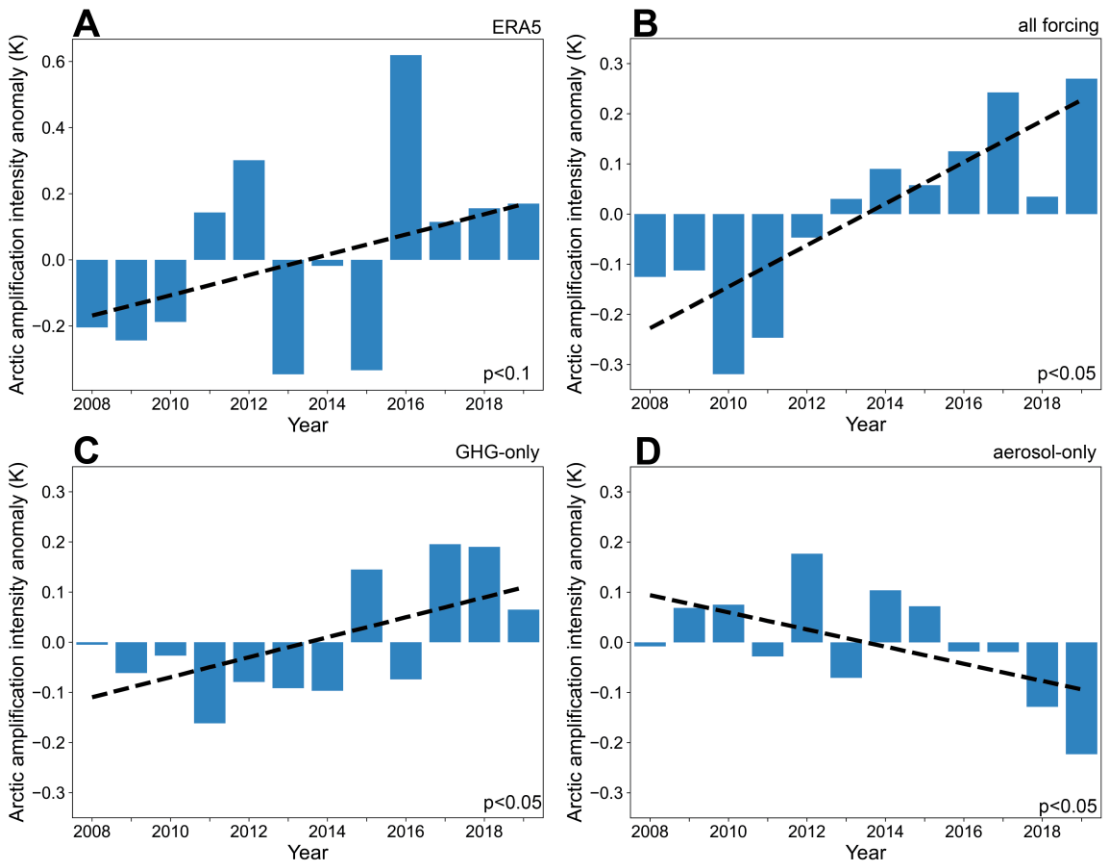

Figure S9. Arctic amplification intensity trend. Time series for Arctic amplification intensity anomalies derived from (A) ERA5, (B) all forcing simulation, (C) GHG-only simulation and (D) aerosols-only simulation over the 2008-2019 period.

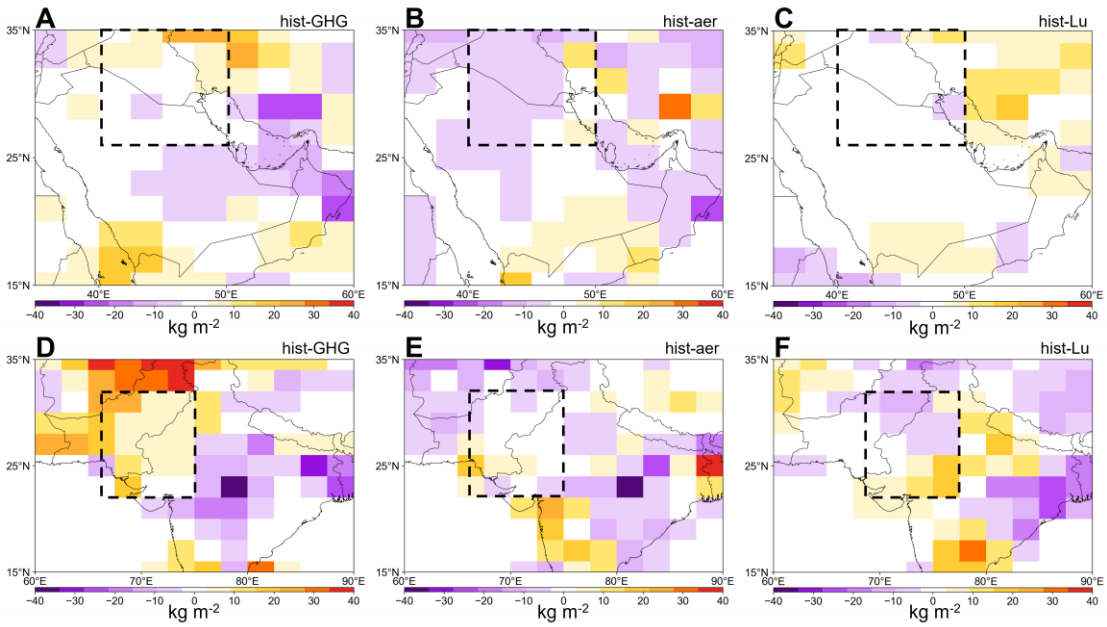

Figure S10. Soil water changes. Spatial distribution of changes in soil water from the Pre-period to the Post-period in West Asia from GHG-only (A), aerosols-only (B) and land use-only forcing (C) experiments. (D), (E) and (F) are in South Asia. Black dashed squares indicate major dust source regions.

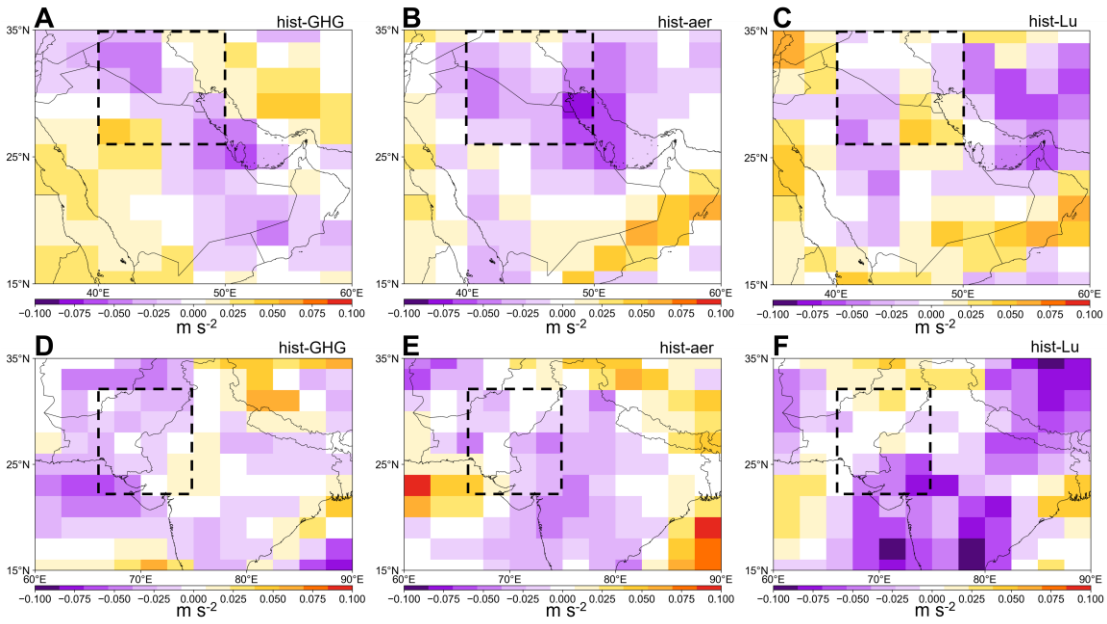

Figure S11. Surface wind speed changes. Spatial distribution of changes in surface wind speed from the Pre-period to the Post-period in West Asia from GHG-only (A), aerosols-only (B) and land use-only forcing (C) experiments. (D), (E) and (F) are in South Asia. Black dashed squares indicate major dust source regions.

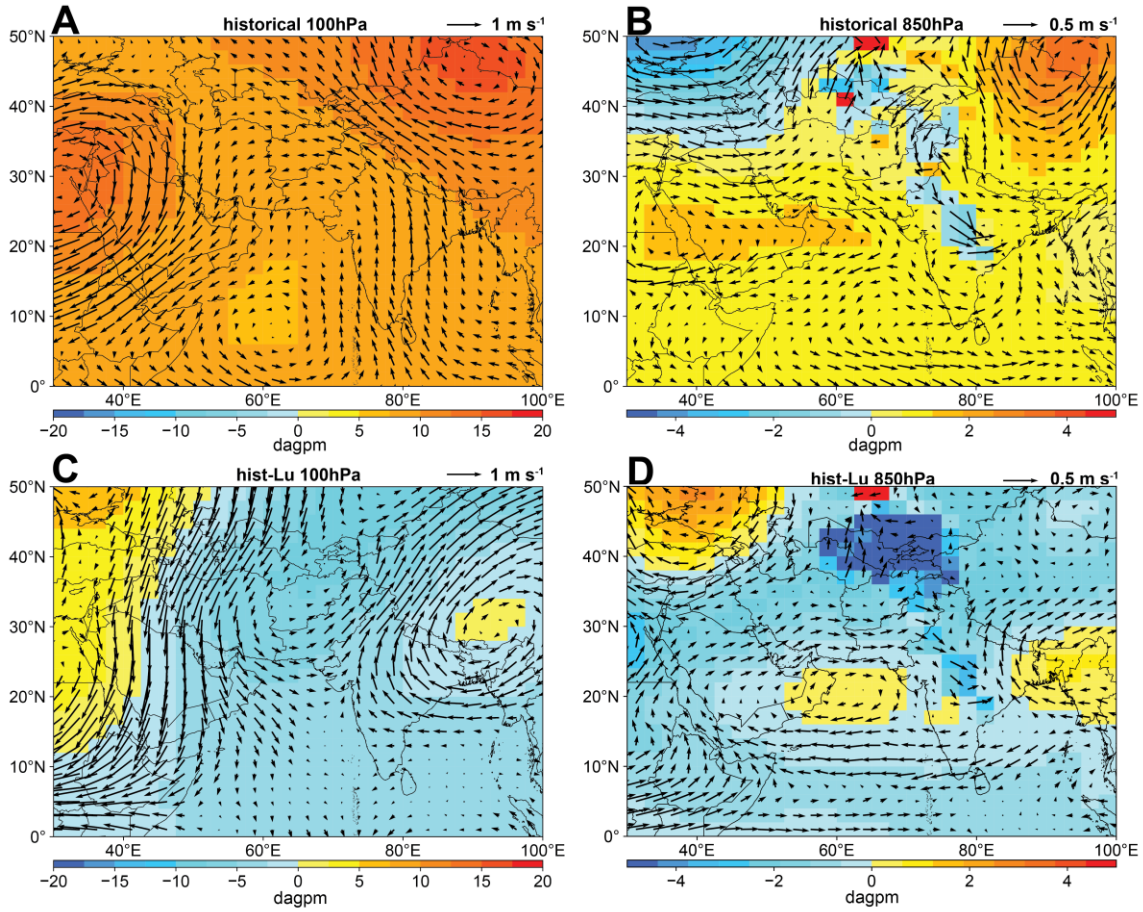

Figure S12. Spatial distribution of geopotential height and atmospheric circulation changes. Spatial distribution of changes in geopotential height and wind from 2008-2011 to 2012-2014 at (A) 100 hPa and (B) 850 hPa from historical all forcing experiments. (C) and (D) are from land use-only forcing experiments.

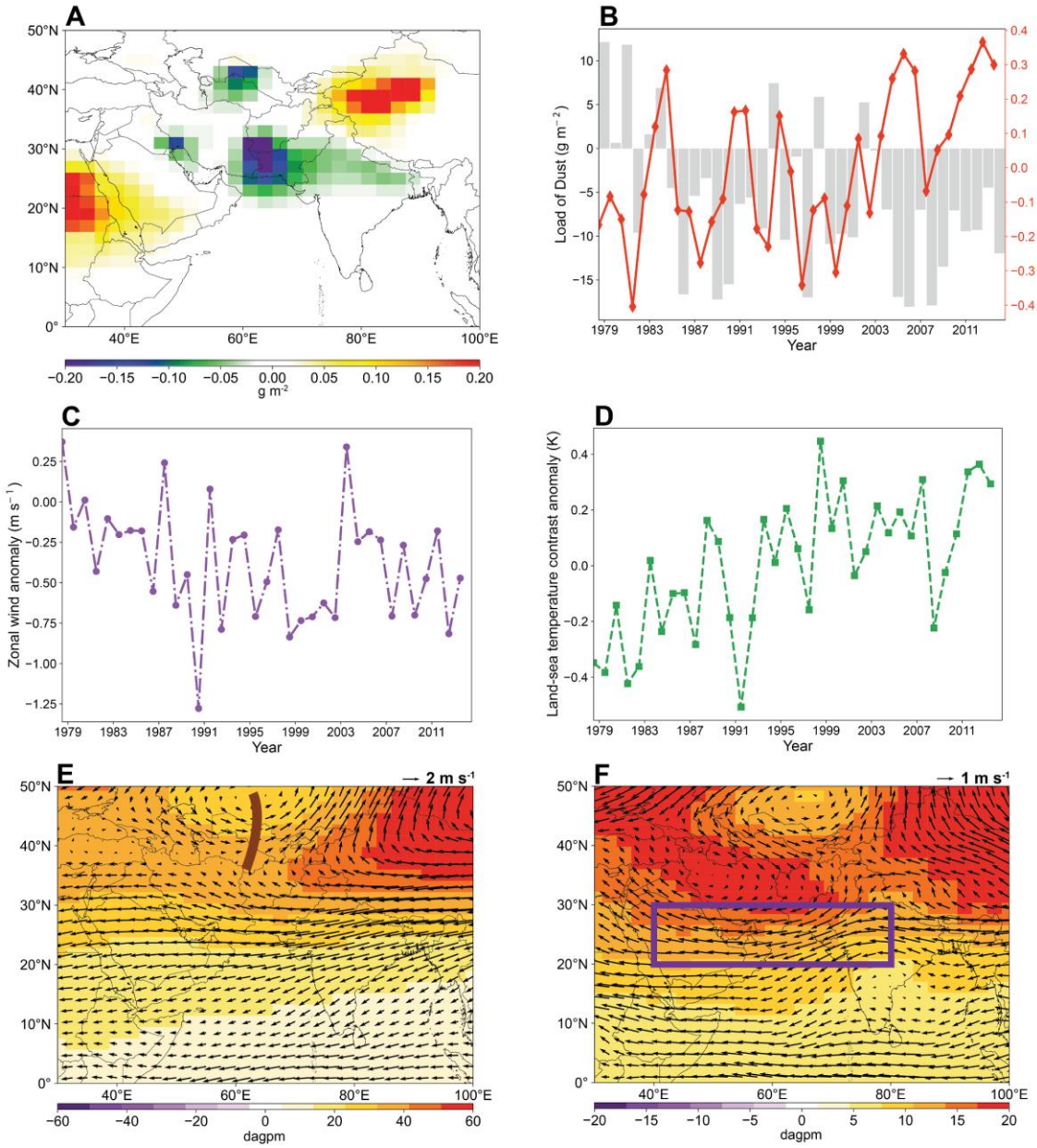

Figure S13. Model simulated responses of dust loading, AAI, land-sea temperature contrast and atmospheric circulation to different amounts of CO_2 concentration. (A) Spatial distribution of difference in the dust loading between AMIP and AMIP-4×CO_2 (AMIP-4×CO_2 minus AMIP). Time series of differences in the dust loading in West and South Asia (land regions enclosed by purple dashed lines in Fig. 1A) and AAI (B), land-sea temperature contrast anomalies (C), and average zonal wind at 850 hPa in the main dust transport region of West and South Asia (purple square in F) (D) between AMIP and AMIP-4×CO_2 (AMIP-4×CO_2 minus AMIP) over the 1979-2014 period. Spatial distribution of difference in geopotential height and wind at (E) 250 hPa and (F) 850 hPa between AMIP and AMIP-4×CO_2 (AMIP-4×CO_2 minus AMIP). The brown line represents the location of trough.

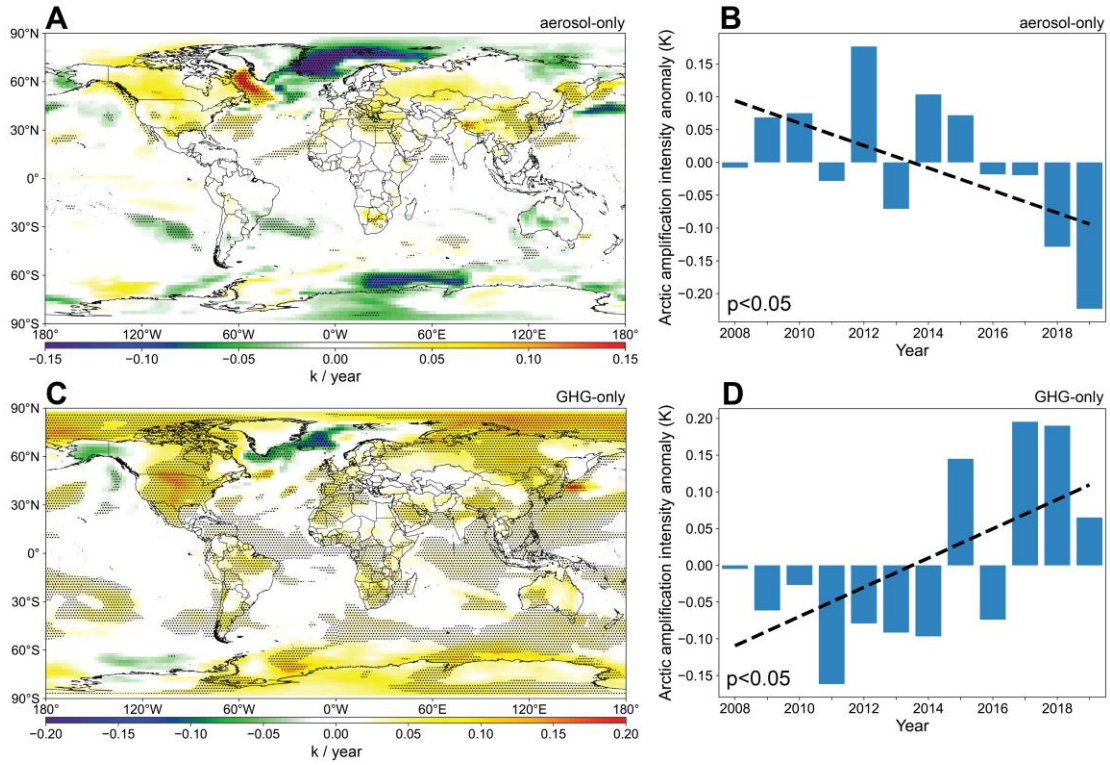

Figure S14. Surface temperature variations. (A) Spatial distribution of surface temperature trend and (B) time series for Arctic amplification intensity anomalies over the 2008-2019 period from aerosols-only forcing experiments. (C) Spatial distribution of surface temperature trend and (D) time series for Arctic amplification intensity anomalies over the 2008-2019 period from GHG-only forcing experiments.

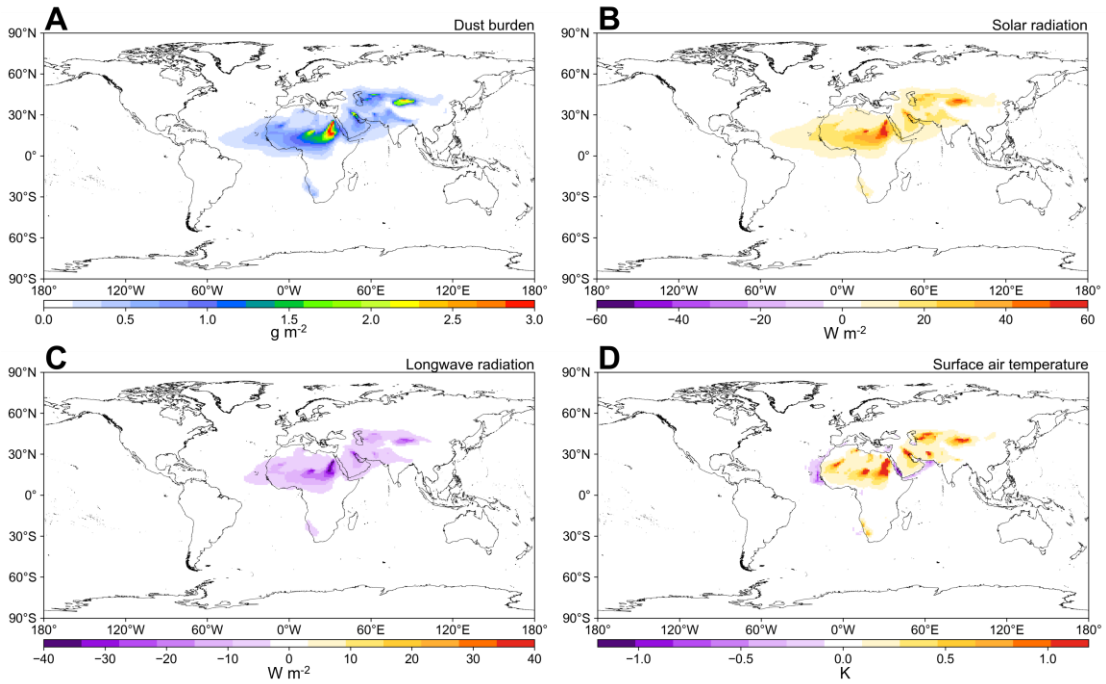

Figure S15. Dust distribution and radiative forcing. (A) Spatial distribution of dust burden. (B) Spatial distribution of changes in downwelling solar radiation at the surface by removing dust radiative effect. (C) Spatial distribution of changes in downwelling longwave radiation at the surface by removing dust radiative effect. (D) Spatial distribution of changes in surface air temperature by removing dust radiative effect.

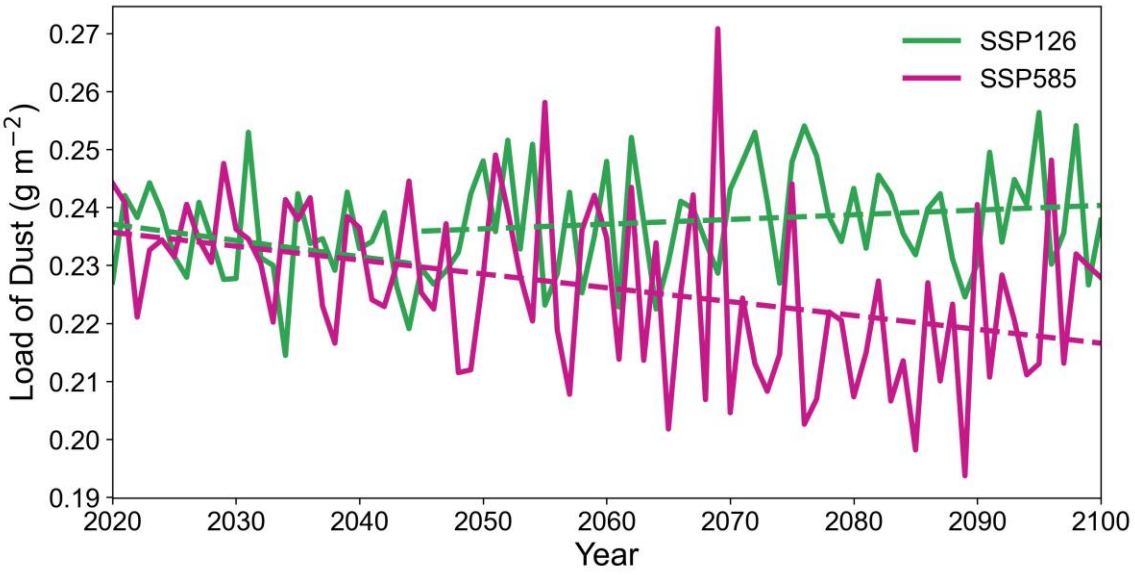

Figure S16. Dust loading under future scenarios. Load of dust over West and South Asia (areas enclosed by purple dashed lines in Fig. 1A) from 2020 to 2100 under the SSP126 and the SSP585 scenarios in CMIP6.

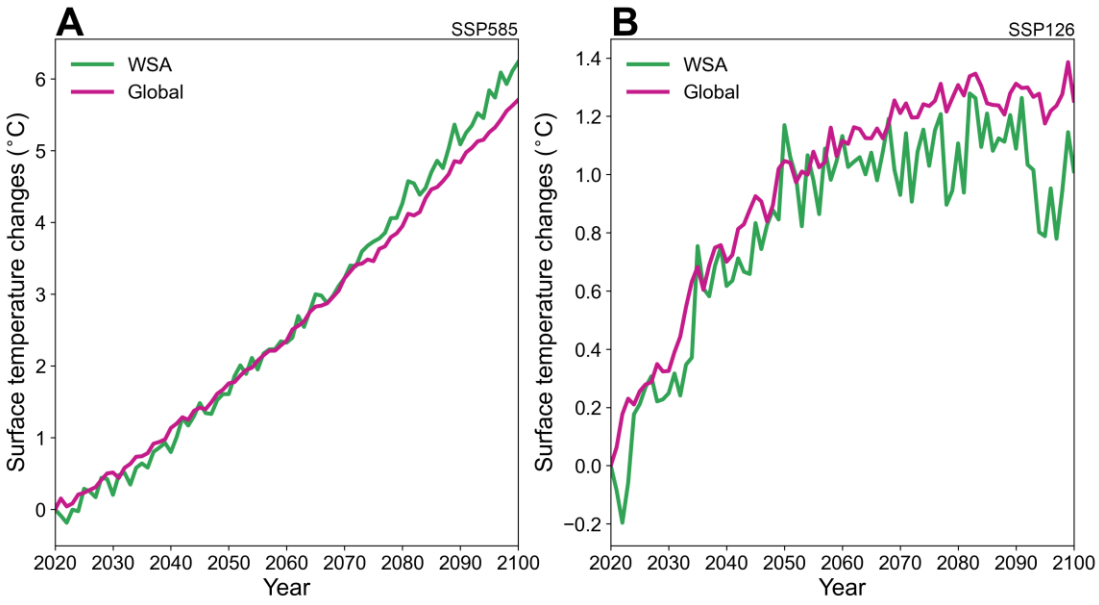

Figure S17. Changes of surface temperature under future scenarios. Changes of surface temperature from 2020 to 2100 in West and South Asia and global under the SSP585 (A) and SSP126 (B) scenarios in CMIP6.

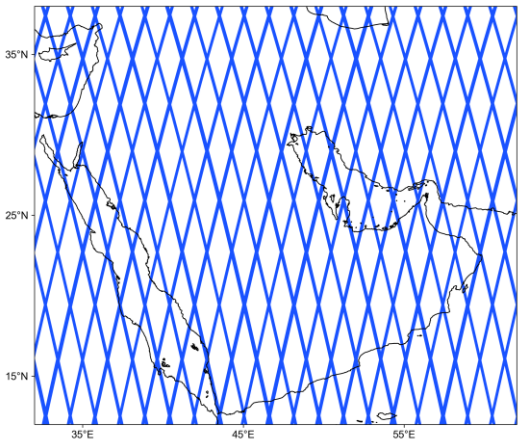

Figure S18. CALIPSO orbit tracks over the Middle East (red square shown in Fig. 2B).

Table S1. A list of CMIP6 models used to evaluate dust responses to GHG-only, aerosols-only and land use-only forcings. GHG-only and aerosols-only forcing simulations are from 2008 to 2019. Land use-only forcing simulations are from 2008 to 2014.

Forcing Name	Model Name	Developer	Resolution (lat × lon)	Reference
GHG-only, aerosols-only	NorESM2-LM	Norwegian Meteorological Institute, Norway	1.875° × 2.5°	Seland, *et al.* (1)
GHG-only, aerosols-only	MIROC6	Atmosphere and Ocean Research Institute, Japan	1.40° × 1.40°	Tatebe, *et al.* (2)
GHG-only, aerosols-only	MRI-ESM2-0	Meteorological Research Institute, Japan	1.125° × 1.125°	Yukimoto, *et al.* (3)
Land use-only	IPSL-CM6A-LR	Institute Pierre-Simon Laplace, France	1.25° × 2.5°	Boucher, *et al.* (4)
Land use-only	MIROC-ES2L	Atmosphere and Ocean Research Institute, Japan	1.40° × 1.40°	Hajima, *et al.* (5)

Table S2. A list of CMIP6 models used to evaluate climate responses to historical all forcing, GHG-only and aerosols-only. All forcing simulations are extended for 2015–2019 using corresponding SSP245 scenario simulations. GHG-only and aerosols-only forcing simulations are from 2008 to 2019.

Model Name	Developer	Resolution (lat × lon)	Reference
ACCESS-CM2	Commonwealth Scientific and Industrial Research, Australia	1.25° × 1.875°	Bi*, et al.* (6)
ACCESS-ESM1-5	Commonwealth Scientific and Industrial Research, Australia	1.25° × 1.875°	Ziehn*, et al.* (7)
BCC-CSM2-MR	Beijing Climate Center, China	1.125° × 1.125°	Wu*, et al.* (8)
CanESM5	Canadian Centre for Climate, Canada	2.815° × 2.815°	Swart*, et al.* (9)
GFDL-ESM4	Geophysical Fluid Dynamics Laboratory, USA	1° × 1.25°	Dunne*, et al.* (10)
GISS-E2-1-G	NASA Goddard Institute for Space Studies, USA	2° × 2.5°	Kelley*, et al.* (11)
IPSL-CM6A-LR	Institute Pierre-Simon Laplace, France	1.25° × 2.5°	Boucher*, et al.* (4)
MIROC6	Atmosphere and Ocean Research Institute, Japan	1.40° × 1.40°	Tatebe*, et al.* (2)
MRI-ESM2-0	Meteorological Research Institute, Japan	1.125° × 1.125°	Yukimoto*, et al.* (3)

Table S3. A list of CMIP6 models used to evaluate climate responses to land use-only forcing. Simulations are from 2008 to 2014.

Model Name	Developer	Resolution (lat × lon)	Reference
ACCESS-ESM1-5	Commonwealth Scientific and Industrial Research, Australia	1.25° × 1.875°	Ziehn, *et al.* (7)
BCC-CSM2-MR	Beijing Climate Center, China	1.125° × 1.125°	Wu, *et al.* (8)
CanESM5	Canadian Centre for Climate, Canada	2.815° × 2.815°	Swart, *et al.* (9)
GFDL-ESM4	Geophysical Fluid Dynamics Laboratory, USA	1° × 1.25°	Dunne, *et al.* (10)
GISS-E2-1-G	NASA Goddard Institute for Space Studies, USA	2° × 2.5°	Kelley, *et al.* (11)
IPSL-CM6A-LR	Institute Pierre-Simon Laplace, France	1.25° × 2.5°	Boucher, *et al.* (4)

Table S4. A list of CMIP6 models used to evaluate dust loading responses to normal and high GHG levels in AMIP setting. Simulated outputs are from 1979 to 2014.

Model Name	Developer	Resolution (lat × lon)	Reference
CESM2	National Center for Atmospheric Research, USA	0.9375° × 1.25°	Danabasoglu*, et al.* (12)
CanESM5	Canadian Centre for Climate, Canada	2.815° × 2.815°	Swart*, et al.* (9)
HadGEM3-GC31-LL	United Kingdom Met Office Hadley Centre, UK	1.25° × 1.875°	Andrews*, et al.* (13)
IPSL-CM6A-LR	Institut Pierre-Simon Laplace, France	1.25° × 2.5°	Boucher*, et al.* (4)
MIROC6	Atmosphere and Ocean Research Institute, Japan	1.40° × 1.40°	Tatebe*, et al.* (2)
NorESM2-LM	Norwegian Meteorological Institute, Norway	1.875° × 2.5°	Seland*, et al.* (1)

Table S5. A list of CMIP6 models used to predict future dust loadings. Simulated outputs are from 2020 to 2100.

Model Name	Developer	Resolution (lat × lon)	Reference
CESM2	National Center for Atmospheric Research, USA	0.9375° × 1.25°	Danabasoglu, *et al.* (12)
CESM2-WACCM	National Center for Atmospheric Research, USA	0.9375° × 1.25°	Gettelman, *et al.* (14)
HadGEM3-GC31-LL	United Kingdom Met Office Hadley Centre, UK	1.25° × 1.875°	Andrews, *et al.* (13)
IPSL-CM6A-LR	Institut Pierre-Simon Laplace, France	1.25° × 2.5°	Boucher, *et al.* (4)
GISS-E2-1-G	NASA Goddard Institute for Space Studies, USA	2° × 2.5°	Kelley, *et al.* (11)
GFDL-ESM4	Geophysical Fluid Dynamics Laboratory, USA	1° × 1.25°	Dunne, *et al.* (10)
UKESM1-0-LL	United Kingdom Met Office Hadley Centre, UK	1.25° × 1.875°	Tang, *et al.* (15)
MRI-ESM2-0	Meteorological Research Institute, Japan	1.125° × 1.125°	Yukimoto, *et al.* (3)

Reference

1. Ø. Seland *et al.*, Overview of the Norwegian Earth System Model (NorESM2) and key climate response of CMIP6 DECK, historical, and scenario simulations. *Geoscientific Model Development* **13**, 6165-6200 (2020).
2. H. Tatebe *et al.*, Description and basic evaluation of simulated mean state, internal variability, and climate sensitivity in MIROC6. *Geoscientific Model Development* **12**, 2727-2765 (2019).
3. S. Yukimoto *et al.*, The Meteorological Research Institute Earth System Model version 2.0, MRI-ESM2. 0: Description and basic evaluation of the physical component. *Journal of the Meteorological Society of Japan. Ser. II* **97**, 931-965 (2019).
4. O. Boucher *et al.*, Presentation and evaluation of the IPSL‐CM6A‐LR climate model. *Journal of Advances in Modeling Earth Systems* **12**, e2019MS002010 (2020).
5. T. Hajima *et al.*, Development of the MIROC-ES2L Earth system model and the evaluation of biogeochemical processes and feedbacks. *Geoscientific Model Development* **13**, 2197-2244 (2020).
6. D. Bi *et al.*, Configuration and spin-up of ACCESS-CM2, the new generation Australian community climate and earth system simulator coupled model. *Journal of Southern Hemisphere Earth Systems Science* **70**, 225-251 (2020).
7. T. Ziehn *et al.*, The Australian earth system model: ACCESS-ESM1. 5. *Journal of Southern Hemisphere Earth Systems Science* **70**, 193-214 (2020).
8. T. Wu *et al.*, BCC-CSM2-HR: a high-resolution version of the Beijing Climate Center Climate System Model. *Geoscientific Model Development* **14**, 2977-3006 (2021).
9. N. C. Swart *et al.*, The Canadian earth system model version 5 (CanESM5. 0.3). *Geoscientific Model Development* **12**, 4823-4873 (2019).
10. J. P. Dunne *et al.*, The GFDL Earth System Model version 4.1 (GFDL‐ESM 4.1): Overall coupled model description and simulation characteristics. *Journal of Advances in Modeling Earth Systems* **12**, e2019MS002015 (2020).
11. M. Kelley *et al.*, GISS‐E2. 1: Configurations and climatology. *Journal of Advances in Modeling Earth Systems* **12**, e2019MS002025 (2020).
12. G. Danabasoglu *et al.*, The community earth system model version 2 (CESM2). *Journal of Advances in Modeling Earth Systems* **12**, e2019MS001916 (2020).
13. M. B. Andrews *et al.*, Historical simulations with HadGEM3‐GC3. 1 for CMIP6. *Journal of Advances in Modeling Earth Systems* **12**, e2019MS001995 (2020).
14. A. Gettelman *et al.*, The whole atmosphere community climate model version 6 (WACCM6). *Journal of Geophysical Research: Atmospheres* **124**, 12380-12403 (2019).
15. Y. Tang *et al.*, MOHC UKESM1. 0-LL model output prepared for CMIP6 CMIP. (2019).